Journal of Applied Crystallography

ISSN 0021-8898

Received 23 November 2007
Accepted 0 XXXXXXX 0000
Online 0 XXXXXXX 0000

A method for the combination of USAXS and SAXS patterns of fibers

Norbert Stribeck[a]* and Ulrich Nöchel[a]

[a]Institute of Technical and Macromolecular Chemistry, University of Hamburg, Bundesstr. 45, D–20146 Hamburg Germany. Correspondence e-mail: Norbert.Stribeck@desy.de

A method for collimation correction and combination of anisotropic scattering patterns recorded in tandem experiments is proposed. It includes both an advanced two-dimensional (2D) extrapolation procedure for the center of the pattern, and (compared to the "blind deconvolution" method) a more justified procedure for desmearing from an unknown broad primary beam profile. This semi-blind deconvolution rests on the availability of unsmeared data in a region of the smeared image.
Materials exhibiting both ultra-small-angle X-ray scattering (USAXS) and small-angle X-ray scattering (SAXS) must be studied in both angular bands (tandem experiment), in order to collect the complete discrete scattering for nanostructure analysis. Merging of the patterns requires desmearing of at least the SAXS pattern from its point-spread function, i.e. the primary beam profile. The distorting effect of single-band experiments on the reconstructed nanostructure of polymer materials is demonstrated.

1. Introduction

Whenever small-angle X-ray scattering (SAXS) patterns are recorded in practice, the profile of the primary beam is non-ideal. This means that a collimation correction is required, in principle. In the classical SAXS literature considerable attention has been paid to the desmearing(Kratky *et al.*, 1951; Synecek, 1960; Ruland, 1964; Glatter, 1974; Deutsch & Luban, 1978; Soliman *et al.*, 1998) of scattering curves. In modern SAXS the smearing is usually disregarded, because the approximation of an ideal point focus is frequently sufficient for the applied methods of data analysis.

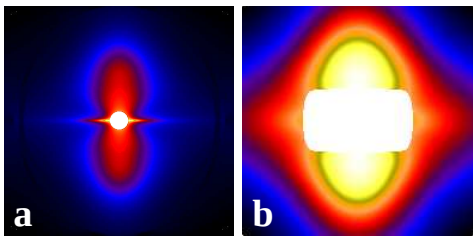

Figure 1
Collimation effect on the scattering pattern of a polypropylene nanofiber measured at different synchrotron beamlines of HASYLAB, Hamburg. **(a)** USAXS pattern measured at beamline BW4. **(b)** SAXS pattern measured at A2. Both images display the same region: -0.05 $nm^{-1} \leq s_1, s_3 \leq 0.05$ nm^{-1}

Nevertheless, desmearing can no longer be avoided, if data must be merged which have been measured with differing primary beam profiles in order to cover the complete angular range in which discrete scattering is observed. Frequently the corresponding materials exhibit both SAXS and ultra-small-angle X-ray scattering (USAXS). Comparing the two patterns, the smeared nature of the SAXS pattern is readily established. Figure 1 demonstrates that pattern merging cannot be successful if the SAXS pattern is not desmeared. As far as we know, a desmearing method for two-dimensional (2D) scattering data has not yet been published.

2. Experimental

2.1. Materials

Different polymer materials are investigated (hard-elastic polypropylene (PP), PP-nanofibers, fibers from polyethylene terephthalate/PP blends) in heat load experiments or during mechanical testing. For the purpose of structure evolution studies, the experiments are monitored by X-ray scattering both in a USAXS setup, and – during a repetition of the experiment – in a SAXS setup ("tandem experiment").

2.2. USAXS

Ultra-small-angle X-ray scattering is performed in the synchrotron beamline BW4 at HASYLAB, Hamburg. The wavelength of radiation is 0.13 nm. The sample-detector distance is ranging between 8 m and 13 m. Scattering patterns are collected by a two-dimensional position sensitive marccd 165 detector (mar research, Norderstedt, Germany) operated in 2048 $\times$ 2048 pixel mode (79 μm quadratic pixel size). Samples are exposed for typically 50 s with a cycle time of 1 min.

2.3. SAXS

Small-angle X-ray scattering is performed in the synchrotron beamline A2 at HASYLAB, Hamburg. The wavelength is 0.15 nm. The sample-detector distance is ranging between 2 m and 3 m. Collection of the scattering patterns is identical to that

IUCr macros version 2.1β1: 2007/05/15

of the USAXS experiment.

2.4. Pre-evaluation

The measured machine background weighted by the absorption factor is subtracted from the raw scattering patterns. Invalid pixels (e.g. behind the beam stop) are discarded. The pattern is aligned by moving its physical center to the center of the image map, rotated so that the fiber axis becomes the vertical axis, and harmonized. The last-mentioned step comprises the filling of missing pixels by utilization of the 4-quadrant symmetry of the fiber pattern. Finally, the scattering intensity is normalized to constant sample thickness by means of the absorption factor as determined from the readings of ionization chamber monitors(Stribeck, 2007*b*).

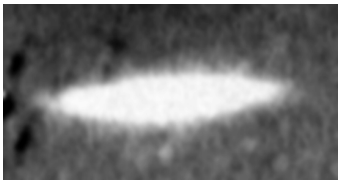

Figure 2
Digitized image of a primary beam profile at beamline A2, HASYLAB. The length of the bright spot is 3 mm

2.5. Primary beam profile

In order to determine the actual primary beam profile, a scintillation screen is provided with a ruler and placed in the position of the detector. The image of the beam spot is monitored by a TV-camera, and a digitized video frame, $W_V(x_1,x_3)$, is obtained. Here x_1 and x_3 are the horizontal and the vertical coordinate of the beam spot image expressed in absolute units of length. Figure 2 shows the raw snapshot of a rather fine primary beam profile recorded at beamline A2 after a good adjustment. In its center $W_V(x_1,x_3)$ is overexposed. Therefore, an analytical model of the beam profile is defined and fitted to the beam profile snapshot. Because the beam shaping is carried out by means of horizontal and vertical slits, the sought point spread function (PSF) is modeled by

$$W(x_1,x_3) = W_1(x_1)\,W_3(x_3) \qquad (1)$$

a product of co-ordinate functions. Moreover, from the calculation of the beamline optics it is known that each of these functions is closely approximated by the shape of a Gaussian.

After a transformation to the units of reciprocal space, $s = (2/\lambda)\sin\theta$ with λ the wavelength of radiation and 2θ the scattering angle, the PSF is

$$W(s_1,s_3) = \frac{1}{2\pi\sigma_1\sigma_3}\exp\left[-\frac{1}{2}\left(\frac{s_1}{\sigma_1}\right)^2\right]\exp\left[-\frac{1}{2}\left(\frac{s_3}{\sigma_3}\right)^2\right], \qquad (2)$$

with s_1 and s_3 the components of the scattering vector **s** in equatorial and meridional direction, respectively. The 2D Fourier transform of $W(s_1,s_3)$ is

$$\begin{aligned} w(r_1,r_3) &= \exp\left(-2\pi^2\sigma_1^2 r_1^2\right)\exp\left(-2\pi^2\sigma_3^2 r_3^2\right) \qquad (3)\\ &= w_1(r_1)\,w_3(r_3)\,. \end{aligned}$$

For the profile presented in Fig. 2 we determine the standard deviations $\sigma_1 = 2.1\,10^{-3}\mathrm{nm}^{-1}$ and $\sigma_3 = 5.9\,10^{-4}\,\mathrm{nm}^{-1}$ in horizontal and vertical direction, respectively.

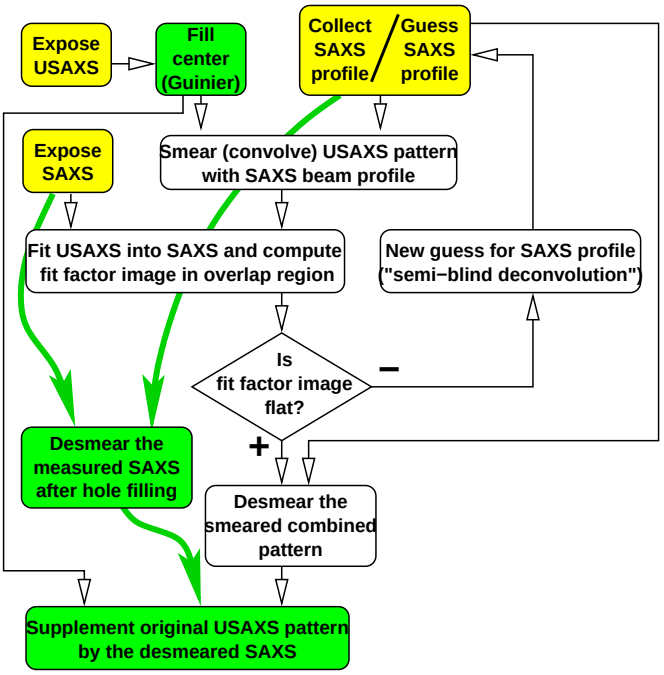

Figure 3
Flow chart of USAXS and SAXS pattern merging combined with collimation correction by desmearing. The straightforward method (curved arrows) suffers from artifacts originating from insufficient hole filling

3. The pattern merging procedure

Figure 3 displays a flowchart both of the obvious straightforward pattern merging procedure (curved arrows), and of a complex pattern merging method proposed by us.

It has been necessary to develop the complex procedure because the simple method is unstable in practice, whereas the complex procedure has proven robust. Thus, it can be utilized for automatic processing of extensive series of scattering patterns from time-resolved experiments. Unfortunately, in the SAXS pattern the blind hole is large, and the data must be desmeared. This is only possible after filling the hole. In the complex procedure the central hole in the SAXS is filled from smeared USAXS data of the same sample in the same state, whereas the simple procedure is based on filling by data extrapolation.

Due to the fact that desmearing is the inversion of an integration, the hole-filling procedure has to return extremely good estimates. Even small errors concerning differentiability will turn into artifacts during desmearing. In the following we present a new 2D extrapolation method. It only appears suitable for filling the beam-stop area of scattering patterns, which do not require desmearing. Later in our data evaluation we use it for filling the hole in the center of the USAXS pattern.

IUCr macros version 2.1β1: 2007/05/15

Beyond that, a new method for the determination of an unknown primary beam profile (i.e. the point-spread function (PSF)) of the SAXS is presented.

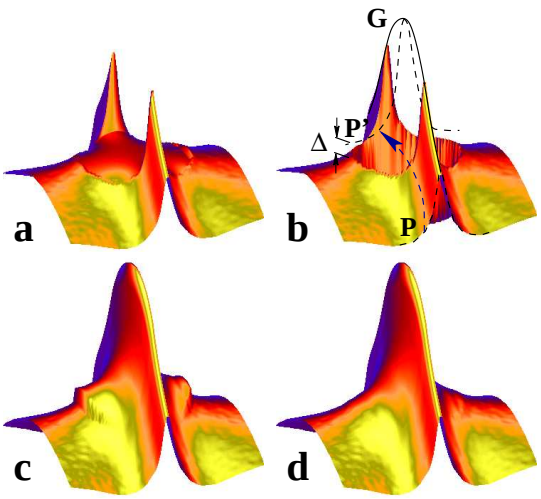

Figure 4
Filling of the central hole. **(a)** The common 2D extrapolation by a "rubber cloth" is only good for filling the hole on a high intensity level. **(b)** The central hole and the concept of filling by a "tent rod" generated by Guinier extrapolation (G), on which another tent rod (P') is moving in transverse direction. The shape of this rod is borrowed from valid data (P). The remaining error Δ is leading to an artificial step. **(c)** The pattern before and **(d)** after error correction by affine transformation of P'

3.1. Improved blind-hole extrapolation

Until recently we have used a standard method for 2D extrapolation. It is based on radial basis functions(Buhmann, 2000; VNI, 2007). Figuratively, the procedure is filling the blind region by some kind of stiffened "rubber cloth". For a direct analysis of the multidimensional chord distribution function (CDF)(Stribeck, 2001) this practice is acceptable. Obviously, it is unsuitable if we have to desmear a scattering pattern. Therefore, we have developed an advanced method which is less prone to produce desmearing artifacts. Figuratively, this procedure is filling the hole by an "igloo tent" supported by bent tent rods. The extrapolation is performed in 3 steps. Figure 4 demonstrates both the previously used method for 2D extrapolation (Fig. 4a), and the new extrapolation procedure.

3.1.1. Step 1 In the first step, two 1D sections (curves) are extracted from the pattern. One curve is extending in meridional, the other in equatorial direction through the center of the pattern. A parabola is fitted to each section. In order to retain some flexibility, an even, 4th-order polynomial is used. The resulting curve closely resembles the beginning of the series expansion of the Guinier extrapolation(Guinier & Fournet, 1955). The section of the two, in which the intensity climbs highest becomes the principal section. In the example (Fig. 4b) the equatorial section is the principal one. The parabolic fit is indicated by a solid line labeled by the letter "G".

3.1.2. Step 2 In the secondary direction, but sufficiently off the blind spot, a complete profile "P" is extracted from the measured data. This profile is put on every pixel of the Guinier-parabola G. Mathematically, the resulting submatrix of intensities in the vicinity of the origin, $I_0'(\mathbf{s})$, is generated by the matrix product of the vectors G and P (`I0P = G # P/MAX(P)`, in the notation of PV-WAVE(VNI, 2007)). Already this 2D intensity distribution, $I_0'(\mathbf{s})$, is a better fill than the rubber cloth (Fig. 4c). Nevertheless, it must be improved because of an artificial step in the resulting data: Let the edge of $I_0'(\mathbf{s})$ which is running parallel to the principal direction be called the correction edge. At the correction edge a step of varying height Δ is observed (Fig. 4b).

3.1.3. Step 3 Let $I_{obs}(\mathbf{s})$ the measured SAXS pattern. Like $I_0'(\mathbf{s})$ it is a matrix, and both matrices are overlapping. After computing the ratio of both matrices in the overlap region, a useful compensation *vector* is extracted along the correction edge of $I_0'(\mathbf{s})$. Each of its elements is the local compensation *factor* for one of the profiles, P', which are hanging down from the G-parabola. Finally, after affine deformation of each of the P' (by multiplication with its local compensation factor), the filling is smoothly approaching the measured data. The result is shown in Fig. 4d. At the former edge of the hole the lacks concerning differentiability are now smaller than after rubber-cloth filling, but not necessarily small enough if we are aiming at desmearing.

The source code of the procedure is in the function sf_i0estimate.pro, which is part of our free program library sf_progs(Stribeck, 2007*a*).

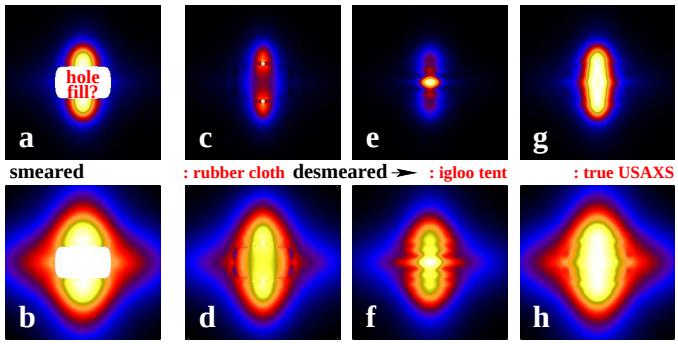

Figure 5
Desmearing artifacts close to the blind hole as a function of the hole-fill procedure in linear intensity scale (top row) and logarithmic scale (bottom row) for hard-elastic PP fiber material. **(a,b)** measured SAXS pattern, central part. Desmearing results after filling the blind hole: **(c,d)** by a rubber cloth; **(e,f)** by the 2D Guinier estimate; **(g,h)** by the smeared USAXS of the same sample

3.2. Hole-fill method compatible with desmearing

A hole-fill method is compatible with desmearing, if it does not introduce perturbing artifacts to the desmeared scattering pattern. This can easily be tested by means of, first, desmearing and, second, inspecting the central part of the desmeared SAXS pattern. Figure 5 demonstrates the differences resulting from different hole-fill methods. The leftmost column (Fig. 5a,b)

IUCr macros version 2.1β1: 2007/05/15

shows the original smeared SAXS in the vicinity of the blind hole. Filled by different methods and desmeared, the results are displayed in the columns to the right.

The next column (Fig. 5c,d) shows the result after filling by the radial-basis-function method (rubber cloth). Considerable distortion is observed inside and outside the former blind spot. The distortion is manifested in strong "over-desmearing", which even causes the apparent intensity to become negative.

Applying the new hole-filling procedure (cf. Fig. 4) to the large SAXS hole, the remnant artifacts are less severe. They no longer cause meaningless intensity values (Fig. 5e,f). Nevertheless, the area of the former hole is full of artificial reflections.

Unfortunately, smooth appearance outside the hole area is not sufficient to guarantee proper desmearing. Only in the next step of data evaluation, in which SAXS and USAXS patterns are merged, it sometimes turns out that there is a mismatch of the slopes in the overlap region. Thus, a more reliable hole-filling method is required.

Finally, if the USAXS pattern is smeared and then taken to fill the SAXS hole (cf. Fig. 4b), the comparison (Fig. 5g,h) shows that inside the blind hole we only observe shallow artificial modulations. Nevertheless, not even these modulations can be taken serious, thus the measured USAXS data must be filled in. Outside the beam-stop area the artifacts are very weak. Consequently, the desmeared SAXS and the USAXS can be matched and merged after simple multiplication by an almost constant factor.

During straight-forward desmearing of SAXS patterns cut-off artifacts are generated close to the edge of the detector, because the measured SAXS intensity has not faded to zero.

In fact, later during analysis the nanostructure information is reduced to a perfectly bandlimited(Stribeck, 2007*b*; Glatter, 1981) function, $G(\mathbf{s})$, which describes the undulation of the scattering intensity about Porod's law. This interference function(Stribeck, 2001) would not suffer from cut-off, but we do not know a way to keep the data numerically stable under the required transforms. Anyway, the cut-off effects can at least be decreased by subjecting the SAXS intensity to cyclic boundary conditions.

In a preceding step, the pixels outside the sensitive circular disk on the detector are filled from extrapolated data in order to obtain a rectangular pattern matrix filled with valid data. For this purpose the rubber-cloth extrapolation(Buhmann, 2000; VNI, 2007) works sufficiently, provided all data points are eliminated that are affected from the penumbra close to the circumference of the vacuum tube.

There is a simple test criterion for the complete elimination of the penumbra region: As long as the penumbra is not eliminated completely, the extrapolated apron is rapidly descending to negative intensity. The penumbra region is readily removed by application of the erode operator(Stribeck, 2007*b*; VNI, 2007; Rosenfeld & Kak, 1982) to the region of valid pixels.

Finally, the pattern is made a periodic function by subjecting it to cyclic boundary conditions. We do not save memory but computing time and put 8 shielding copies of the image around the central scattering pattern. After each iteration we restore integrity by copying the central tile onto all its outward neighbors. Programmed this way in PV-WAVE(VNI, 2007), loops are avoided. This assures fast desmearing without visible artifacts at the edge of the intensity matrix.

3.3. Smearing and desmearing

Before we start to describe the desmearing procedure itself, a brief summary of the well-known(Alexander, 1979; Glatter & Kratky, 1982; Baltá Calleja & Vonk, 1989; Stribeck, 2007*b*) mathematical background shall be given. The measured scattering pattern, $I_{obs}(s_1,s_3)$, appears smeared because of imperfect collimation quantified by the point-spread function (PSF) $W(s_1,s_3)$. Its relation to the ideal intensity sought after, $I(s_1,s_3)$, is given by the correlation integral

$$I_{obs}(s_1,s_3) = \int_{-\infty}^{\infty} I(y_1,y_3)\,W(s_1+y_1,s_3+y_3)\,dy_1dy_3 \quad (4)$$

$$:= I(s_1,s_3) \star W(s_1,s_3)\,. \quad (5)$$

Correlation is equivalent to convolution, if at least one of its partners is an even function, e.g. $W(\mathbf{s}) = W(-\mathbf{s})$. Inversion of Eq. (4) is carried out either directly, or by iteration. The direct inversion by means of Fourier transforms

$$I(\mathbf{s}) = \mathscr{F}_2^{-1}(\mathscr{F}_2(I_{obs}(\mathbf{s}))/\mathscr{F}_2(W(-\mathbf{s}))) \quad (6)$$

$$= \mathscr{F}_2^{-1}(\mathscr{F}_2(I_{obs}(\mathbf{s}))/w(-\mathbf{r}))\,. \quad (7)$$

has first been proposed by Stokes(Stokes, 1948), and is a corollary of the Fourier-slice theorem(Stribeck, 2007*b*). In the equation let $\mathbf{s} = (s_1,s_3)$. $\mathscr{F}_2()$ designates the two-dimensional Fourier transform, the back-transform of which is realized by the operator $\mathscr{F}_2^{-1}()$. $w(\mathbf{r})$ is referring to Eq. (3).

The iterative desmearing is, in general, implemented by variants of the method devised by v. Cittert(Burger & van Cittert, 1932; Ergun, 1968; Glatter, 1974). The variants differ in the way, in which the correction function is smoothed – a function which is computed in each iteration step. In the common algorithm of Glatter(Glatter, 1974) the smoothing is performed by convolution with a triangle. Modern signal processing manuals(VNI, 2007) recommend the use of an adapted digital filter. As recommended, we utilize a 10th order adapted digital filter with standard parameters from the library of PV-WAVE(VNI, 2007).

The principle of the iterative desmearing is based on the obvious fact that the correlation of the sought-after intensity, $I(\mathbf{s})$, with the primary beam profile, $W(\mathbf{s})$, is broadening the signal $I_{obs}(\mathbf{s})$. Now the simple idea is to smear the already smeared signal $I_{obs}(\mathbf{s})$ a second time, then to determine the resulting intensity variation at each point of the pattern yielding a correction function, and – after the above-mentioned smoothing step – to invert the variation in order to obtain an improved guess of the sought function. Evidently, this principle can be iterated and convergence is found after m iterations if the guess intensity $I^m(\mathbf{s})$ smeared by $W(\mathbf{s})$

$$I^m(\mathbf{s}) \star W(\mathbf{s}) = I_{obs}(\mathbf{s}) \quad (8)$$

is equal to the measured intensity.

IUCr macros version 2.1β1: 2007/05/15

3.4. SAXS desmearing

After the pre-evaluation of the SAXS patterns has been described and the two deconvolution methods have been sketched, let us now turn to the selection of the deconvolution method itself.

3.4.1. The direct method As we are modeling the actual PSF by a model (cf. Eq. (2) and Eq. (3)), we can save a numerical Fourier transform as we utilize Eq. (7). Nevertheless, the division in Fourier space leads to a serious problem, because it is strongly amplifying noise in the outer part of the matrix, and similar noise is observed in the "desmeared" function(Deng *et al.*, 2003). The square of the mentioned matrix is the power spectrum of the scattering pattern. If $I_{obs}(\mathbf{s})$ could be made bandlimited as in the area of tomography(Deng *et al.*, 2003) or in crystallography(Ida & Toraya, 2002), acceptable results could perhaps be obtained by adaption of a low-pass filter applied in Fourier space.

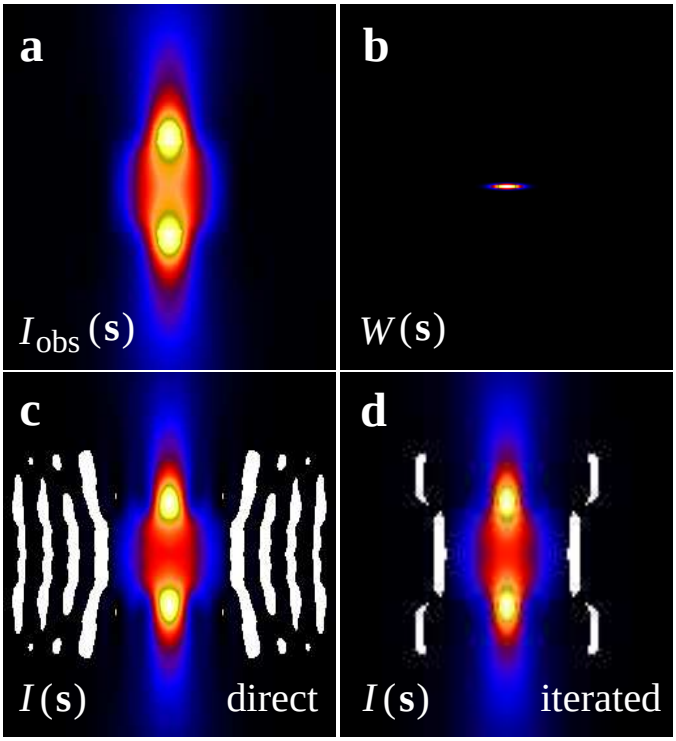

Figure 6
Comparison of direct and iterated desmearing algorithms. SAXS pattern of a polypropylene fiber. The images show the extracted region -0.045 $\mathrm{nm}^{-1} \leq s_1, s_3 \leq 0.045\ \mathrm{nm}^{-1}$

Our directly desmeared patterns always show both discrete artifacts where the intensity is low, and – even worse – incomplete desmearing. The data are unsuitable for structure analysis. Figure 6 shows the SAXS pattern of a polypropylene fiber before and after desmearing. For the purpose of artifact demonstration, the central blind spot has been filled by the poor rubber-cloth extrapolation.

Figure 6c shows the result of the direct deconvolution. It has already been optimized by individual adaption of the low-pass filter, but such manual optimization cannot be tolerated, as we are aiming at the automatic processing of extensive series of patterns. Moreover, the complete region of low intensities is filled with artificial ripples, and the desmearing effect in the main peaks is clearly limited by the distorting effect of the low-pass filter.

3.4.2. The iterative method A representative result of the iterative method is shown in Fig. 6d. The general result can be accepted because of the built-in check used in the convergence test. Compared to Fig. 6c the reflections are narrower indicating that desmearing achieved by the direct method has been incomplete. Nevertheless, even the result of the iterative method shows artifacts. Due to the fact that they are localized at the border of the filled central hole, they are readily attributed to improper hole-filling.

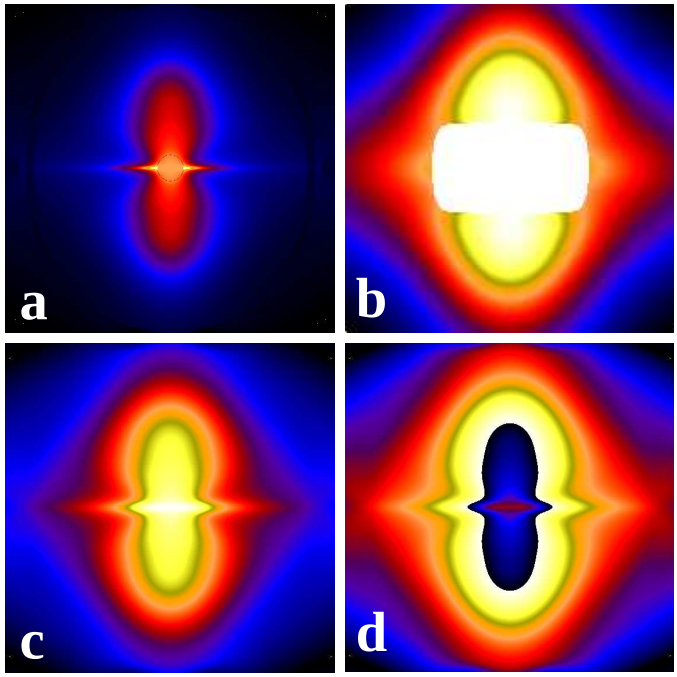

Figure 7
a) USAXS pattern of a PP nanofiber measured at BW4. **b)** The same sample measured at A2. **c)** Pattern (a) smeared with the actual beam profile of beamline A2. **d)** (b) filled with (c)

3.5. Filling by smeared USAXS and semi-blind deconvolution

Figure 7 demonstrates the filling of the central hole for a studied polypropylene nanofiber. This example is extreme, because the USAXS of the material is particularly distinct (Fig. 7a). Moreover, the adjustment of the beamline optics has been rather poor during the measurement of the SAXS (Fig. 7b). The scattering pattern of Fig. 7c is obtained by smearing of the measured USAXS pattern with the primary beam profile of the SAXS according to Eq. (4). It is readily fitted into the hole of the measured SAXS pattern. The result is shown in Fig. 7d.

In order to merge the patterns, the average fit factor is computed from the region, where both SAXS data and USAXS data are present.

IUCr macros version 2.1β1: 2007/05/15

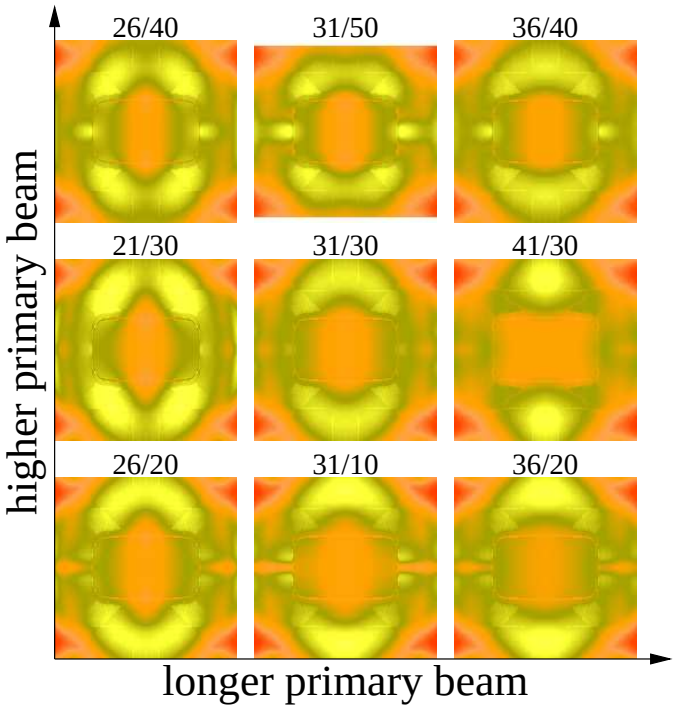

Figure 8
Demonstration of the semi-blind deconvolution approach in the desmearing procedure (Fig. 3): Choose the size of the primary-beam profile that flattens the image of fill factors best. Images of the fill-factor are presented in pseudo-color as a function of width, σ_1, and height, σ_3, of the profile. The labels indicate the pairs σ_1/σ_3 in units of 10^{-4}nm^{-1} in reciprocal space

Moreover, even an individual fit factor for each pixel in the overlap zone can be computed. The result is a fill-factor matrix. The variation of this fill-factor matrix as a function of primary-beam length and height is shown in Fig. 8. The fill-factor matrix in the center of the figure is the flattest, because there the parameters of the real PSF of the SAXS, $\sigma_1 = 3.1 \times 10^{-3}$ nm^{-1} and $\sigma_3 = 3 \times 10^{-3}$ nm^{-1}, are used. Admittedly, even in this matrix shallow local maxima and minima are observed. Nevertheless, both the amplitude between the highest peak and the lowest valley is smallest, and the peaks and the valleys are broader compared to the other fit factor matrices. Deviation from the optimum leads to an increasingly wavy fill factor image. Thus, the flatness of the fill-factor matrix appears to be a suitable criterion for having chosen a primary beam profile of proper width and height. In this way a suitable SAXS-PSF, $W(\mathbf{s})$, can be determined even if it has not been measured. After the determination, the SAXS pattern is desmeared using this PSF. We call this PSF-search method a "semi-blind" deconvolution in contrast to the PSF search in the blind deconvolution that depends on the detection of over-desmearing.

In detail, as the beam is made longer and longer (Fig. 8, middle row), the fill-factor matrix is compensating this change by lifting the main peaks. On the other hand, as the primary beam height is increased (middle column), the overcompensation of the equatorial streak first is corrected and then lifted above the average fill factor. After understanding this mechanism, the direction of optimization can already be determined after the first test with some starting values for length and height of the primary beam.

4. Results and discussion

Whenever both SAXS and USAXS exhibit discrete scattering ("double-band scattering"), SAXS and USAXS should be merged, as long as there is no special reason to focus on only part of the nanostructure information offered by the material's scattering.

If in this case only one of the experiments is carried out ("single-band experiment"), the results of nanostructure analysis will be biased. Pure SAXS returns low-pass-filtered structure information, whereas the features accessible from the USAXS experiment will result in an image of the nanostructure that emphasizes the longer-ranging structural features from the high-pass-filtered structure information of its pattern.

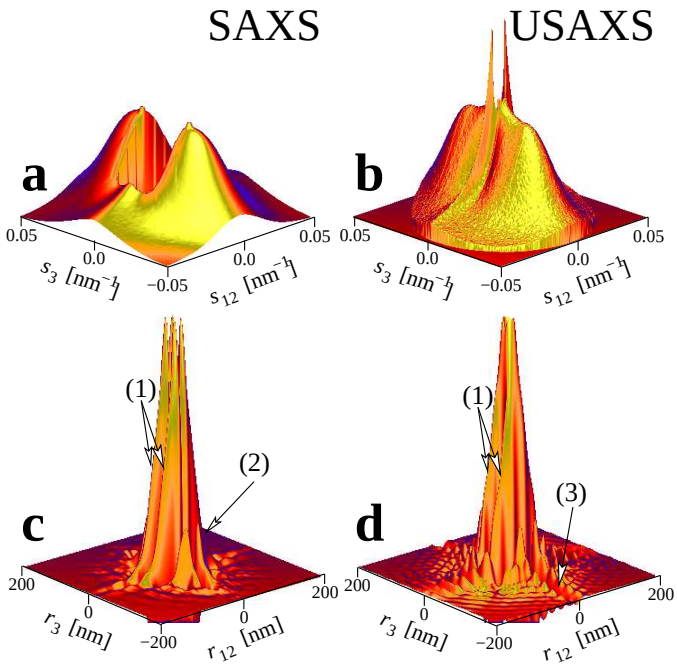

Figure 9
PP fiber. Comparison of the results of single-band SAXS and USAXS experiments. All data on a logarithmic scale. **(a,b)**: Scattering data **(c,d)**: The corresponding CDFs computed separately from each pattern. The sensitivity of each pattern to the features of the nanostructure is different: (1) The first pair of triangular peaks indicates layer structure. (2) The second order indicates stacks of layers. (3) The meridional streak indicates needle-shaped domains extending in fiber direction

4.1. Polypropylene fiber

Clear double-band scattering is shown by a hard-elastic polypropylene fiber (Fig. 9a,b). The plot (Fig. 9a) displays only the central part of the recorded SAXS. The USAXS data (Fig. 9b) show that the blind spot is so large that an essential fraction of the discrete scattering is still missing. On the contrary, the USAXS provides the scattering inside the blind spot, but not the higher orders of the main SAXS reflections.

If we take each part for the whole and compare the results, both matches and differences are observed. For the purpose of

IUCr macros version 2.1β1: 2007/05/15

demonstration the nanostructure computed from each single-band experiment is displayed in real space by means of the multi-dimensional chord distribution function (CDF)(Stribeck, 2001; Stribeck, 2007*b*) (Fig. 9c,d).

Obviously, the long period and the average layer thickness (label (1) in the graphs) can be extracted from both patterns with little difference. Nevertheless, the advanced topological information is quite different. From the SAXS-CDF weak correlation among neighboring lamellae would be deduced (Label (2)) which is not visible in the USAXS. On the other hand, only the USAXS-CDF clearly shows the counterpart of the equatorial streak (Label (3)).

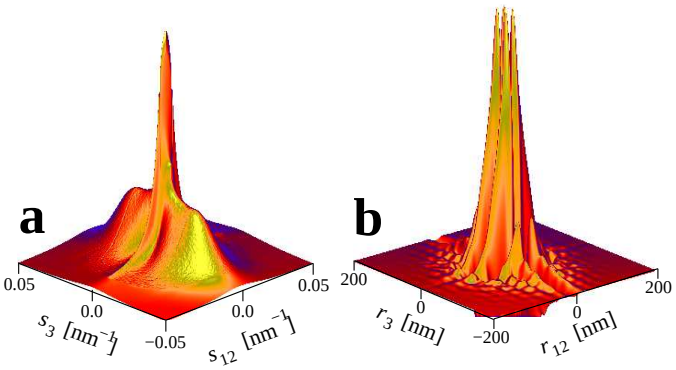

Figure 10
After pattern merging. **(a)** the inner part of the scattering merged from USAXS and SAXS. In the center the filling of the small USAXS hole by the novel extrapolation method is visible. The outward part of the pattern originates from the desmeared SAXS. **(b)** The CDF computed from the merged scattering pattern shows a combination of all the nanostructural features observed in Figs. 9c,d and a reduced level of artifacts

The result of merging USAXS and SAXS by means of the new method is shown in Fig. 10a. Obviously, the novel 2D extrapolation method yields an acceptable intensity shape in the vicinity of zero scattering angle, when applied to fill the small central hole in the USAXS. Moreover, in the transition region between USAXS and SAXS even in the presented logarithmic scaling neither a step nor a sudden change of slope is observed.

The CDF obtained from the merged pattern is shown in Fig. 10b. In this CDF from the double-band (i.e. SAXS and USAXS) experiment the nanostructural features of the previously discussed single-band CDFS are combined: Both the weak correlation among the lamellae, and the meridional double-ridge related to the needle-shaped domains which generate the equatorial streak in the USAXS are observed.

4.2. Polypropylene nanofiber

Finally, we present a material with even more pronounced discrete scattering in both angular ranges. Correspondingly, the filter effect of single-band experiments becomes even stronger. Similar effects can be expected with other ordered nanostructured polymeric materials that presently are in the focus of research.

For such materials even cursory inspection of the SAXS scattering pattern clearly exhibits that the recorded data are incomplete, because not only part of the equatorial streak, but also part of the long period reflection are masked by the beam stop. On the other hand, if the USAXS is recorded first, the missing higher orders of the long period reflection may be overlooked.

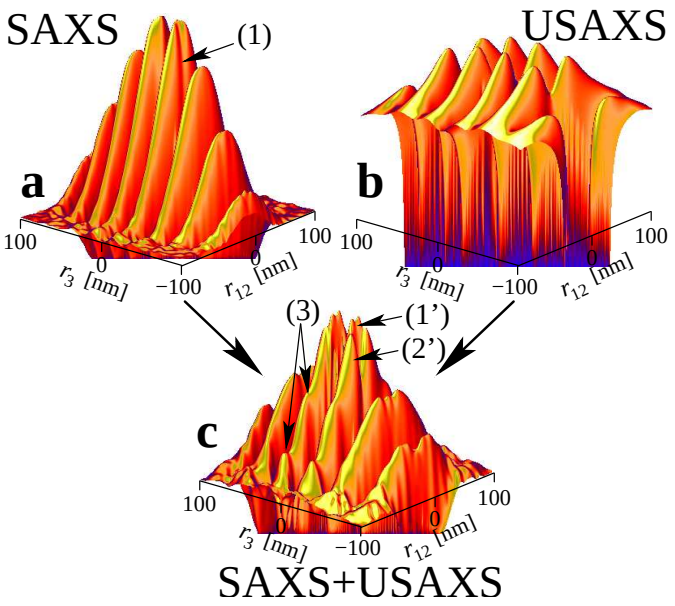

Figure 11
PP nanofiber material. Nanostructure information extracted from the SAXS pattern, the USAXS pattern and the merged scattering pattern. The Real-space CDFs are trimmed to the same region, respectively.

Without resorting to the scattering patterns, let us directly demonstrate the effect of band-pass filtering on the CDF nanostructure image. Figure 11a exhibits the nanostructure of a pure lamellae system. The layer thickness distribution appears to be rather broad. Only a shallow groove (Fig. 11a, (1)) is indicating that the material might be made from stacks of finite lamellae with some transverse offset.

On the other hand, the USAXS CDF (Fig. 11b) presents a nanostructure which is dominated by the effect of needle-shaped domains oriented in fiber direction (r_3). For the purpose of direct comparison we have chosen to display the same region of real space in all plots. Based on Fig. 11b we cannot discuss the details of the needle structure, but the peaks forming triangles in equatorial direction (r_{12}) are clearly visible and demonstrate that even the single-band USAXS is noticing some of the features of the lamellae system.

Finally, the CDF based on the merged data (Fig. 11c) is displaying the complexity of the nanostructure of this material in high spatial resolution. Triangles(Stribeck, 2001) of narrow extension in fiber direction are characterizing lamellae of rather uniform thickness (Fig. 11c (1′)). The bulky peaks in front of them (2′) which are split at the meridian are identified by thicker layers in between with a broad thickness variation, and the splitting is resulting from individual transverse offset(Stribeck *et al.*, 2005; Keum *et al.*, 2005) among the other layers, i.e. the ones of well-defined thickness. Consequently, the crystalline layers (1′) now appear distinguishable from the amorphous gaps (2′) between them.

IUCr macros version 2.1β1: 2007/05/15

Besides that, the modulation of the triangular layer peaks (Fig. 11c (3)) is indicating that the lamellae are either made from blocks(Hugel *et al.*, 1999), or that a cross-hatched structure(Olley & Bassett, 1989) is present. The explanation which is more probable can be deduced from the structure evolution during heat-treatment of the material, which has not yet been published.

The completeness of the double-band data would be guaranteed, if we could verify that outside the limits of the combined angular band sensed in our experiments (0.001 nm^{-1} $< |\mathbf{s}| <$0.3 nm^{-1}) there were no discrete scattering. In this case even an extension of the angular bandwidth would not further clarify the perception of nanostructure.

5. Conclusion and outlook

The discrete modulation of the intensity measured in a scattering experiment is, in principle, the power spectral density of the information on the nanostructure topology. We assume that this information is bandlimited. In case the bandwidth of the studied material is wider than the angular band of the instrument employed, alteration of the reconstructed nanostructure cannot be avoided. In this paper we have proposed a method that can be used to minimize the corresponding shift by means of tandem experiments, desmearing, and merging of the scattering patterns.

In order to avoid the proposed complex procedure one might think of increasing the angular bandwidth of the instrument by employing both a microbeam and a large-area high-resolution detector(Riekel, 2000). In such a setup USAXS and SAXS would be recorded simultaneously. Nevertheless, a new problem is arising with such a setup from the steep fall-off of the scattering intensity and the necessity to collect low-noise data over the complete angular range. In the case of static measurements and if a detector with high (or cyclic) dynamics were at hand, one simply could wait until even at high angles enough photons were collected. On the other hand, longer exposure is no solution if structure evolution shall be studied *in situ*. In this area of research the available devices even for the singeband setup are still slow. Thus, tandem experiments carried out at dedicated synchrotron beamlines appear to be a serious option for the investigation of nanostructure evolution of complex polymer materials.

Another pathway may become viable, as detector technology and data treatment are advancing. With the novel PILATUS detector technology(Broennimann *et al.*, 2006) large-area detectors with a short readout time can be realized, and by application of 3D adapted smoothing technique it may become possible to produce low-noise sequences of double-band scattering data with high time resolution in a single experiment – a microbeam-setup with a large, fast and effective high-resolution detector. The addressed 3D smoothing procedure would resort to the elapsed time, t, as the 3rd dimension considering the measured intensity $I(s_{12}, s_3, t)$ a function of 3 variables. Adaption could be realized by increasing the number of considered pixels for smoothing with increasing distance $\left(s_{12}^2 + s_3^2\right)^{0.5}$ from the center of the pattern.

We thank the Hamburg Synchrotron Radiation Laboratory (HASYLAB) for beam time granted in the frame of project II-01-041. We are in particular obliged to the beamline scientists S. S. Funari and A. Timmann for their support. We gratefully acknowledge funding by the Deutsche Forschungsgemeinschaft, project STR 501/4-2.

References

Alexander, L. E. (1979). *X-Ray Diffraction Methods in Polymer Science*. New York: Wiley.

Baltá Calleja, F. J. & Vonk, C. G. (1989). *X-Ray Scattering of Synthetic Polymers*. Amsterdam: Elsevier.

Broennimann, C., Eikenberry, E. F., Henrich, B., Horrisberger, R., Hülsen, G., Pohl, E., Schmitt, B., Schulze-Briese, C., Suzuki, M., Tomizaki, T., Toyokawa, A. & Wagner, A. (2006). *J. Synchrotron Rad.* **13**(2), 120–130.

Buhmann, M. D. (2000). *Acta Numerica*, **9**, 1–38.

Burger, H. C. & van Cittert, P. H. (1932). *Z. Phys.* **79**(12), 722.

Deng, Y., He, G., Kuppusamy, P. & Zweier, J. L. (2003). *Magn. Reson. Med.* **50**(2), 444–448.

Deutsch, M. & Luban, M. (1978). *J. Appl. Cryst.* **11**, 98–101.

Ergun, S. (1968). *J. Appl. Cryst.* **1**(1), 19–23.

Glatter, O. (1974). *J. Appl. Cryst.* **7**, 147–153.

Glatter, O. (1981). *J. Appl. Cryst.* **14**, 101–108.

Glatter, O. & Kratky, O. (eds.) (1982). *Small Angle X-ray Scattering*. London: Academic Press.

Guinier, A. & Fournet, G. (1955). *Small-Angle Scattering of X-Rays*. London: Chapman and Hall.

Hugel, T., Strobl, G. & Thomann, R. (1999). *Acta Polym.* **50**, 214–217.

Ida, T. & Toraya, H. (2002). *J. Appl. Cryst.* **35**(1), 58–68.

Keum, J. K., Burger, C., Hsiao, B. S., Somani, R., Yang, L., Chu, B., Kolb, R., Chen, H. & Lue, C.-T. (2005). *Progr. Colloid Polym. Sci.* **130**, 113–125.

Kratky, O., Porod, G. & Kahovec, L. (1951). *Z. Elektrochemie*, **55**(1), 53–59.

Olley, R. H. & Bassett, D. C. (1989). *Polymer*, **30**(3), 399–409.

Riekel, C. (2000). *Rep. Prog. Phys.* **63**(3), 233–262.

Rosenfeld, A. & Kak, A. C. (1982). *Digital Picture Processing*, vol. 1. London: Academic Press.

Ruland, W. (1964). *Acta Cryst.* **17**(2), 138–142.

Soliman, M., Jungnickel, B.-J. & Meister, E. (1998). *Acta Cryst., Sect. A: Found. Cryst.* A**54**(5), 675–681.

Stokes, A. R. (1948). *Proc. Phys. Soc.* **61**, 382–391.

Stribeck, N. (2001). *J. Appl. Cryst.* **34**(4), 496–503.

Stribeck, N., (2007*a*). Downloads. http://www.chemie.uni-hamburg.de/tmc/stribeck/dl.

Stribeck, N. (2007*b*). *X-Ray Scattering of Soft Matter*. Heidelberg, New York: Springer.

Stribeck, N., Bösecke, P., Bayer, R. & Almendarez Camarillo, A. (2005). *Progr. Coll. Polym. Sci.* **130**, 127–139.

Synecek, V. (1960). *Acta Cryst.* **13**, 378–380.

VNI, (2007). Pv-wave manuals. V 7.5, Boulder, Colorado.

Synopsis

Combination of two-dimensional scattering patterns measured with different instruments requires collimation correction. The method is demonstrated by SAXS and USAXS of polymer fiber materials